Nanoscale

In situ studies on defects formation dynamics in flash-sintered TiO_2

Journal:	*Nanoscale*
Manuscript ID	NR-ART-06-2023-002630.R1
Article Type:	Paper
Date Submitted by the Author:	18-Aug-2023
Complete List of Authors:	Xue, Sichuang; Xi'an Jiaotong University, StateKey Laboratory for Mechanical Behavior of Materials Phuah, Xin; Purdue University, School of Materials Engineering Jian, Jie; Harbin Institute of Technology Shenzhen, Institute of Special Environments Physical Sciences Li, Qiang; Purdue University System, School of Materials Engineering Li, Jin; Harbin Institute of Technology Shenzhen, Institute of Special Environments Physical Sciences Yang, Bo; Purdue University System Zhang, Di; Purdue University System, School of Materials Engineering Wang, Han; Purdue University, School of Materials Engineering Tsakalakos, Thomas; Rutgers University, Department of Materials Science and Engineering Mukherjee, Amiya; University of California, Department of Chemical Engineering & Materials Science Wang, Haiyan; Purdue University System, MSE; Neil Armstrong Engineering Building Zhang, Xinghang; Purdue University System, Materials Engineering

In situ studies on defects formation dynamics in flash-sintered TiO_2

Sichuang Xue [a,b]*, Xin Li Phuah [b], Jie Jian [c], Qiang Li [b], Jin Li [c], Bo Yang [b], Di Zhang [b], Han Wang [b], Thomas Tsakalakos [d], Amiya K. Mukherjee [e], Haiyan Wang [b, f]*, Xinghang Zhang [b]*

[a] *StateKey Laboratory for Mechanical Behavior of Materials, Xi'an Jiaotong University, Xi'an 710049, China*
[b] *School of Materials Engineering, Purdue University, West Lafayette, IN 47907, USA*
[c] *Institute of Special Environments Physical Sciences, Harbin Institute of Technology, Shenzhen, 518055, P.R. China*
[d] *Department of Materials Science and Engineering, Rutgers University, New Brunswick, NJ 08901, USA*
[e] *Department of Materials Science and Engineering, University of California, Davis, CA 95616, USA*
[f] *School of Electrical and Computer Engineering, West Lafayette, IN 47907, USA.*

*Corresponding authors: Sichuang.xue@xjtu.edu.cn; Xinghang Zhang, xzhang98@purdue.edu; Haiyan Wang, hwang00@purdue.edu

Abstract

Flash-sintered (FS) ceramics have shown promising mechanical deformability at room temperature comparing to conventional sintered ceramics. One major contributing factor to plasticity is the high-density defects, such as dislocations, stacking faults and point defects, resulted presumably from the high electrical field during flash sintering. However, *in situ* evidence for the defect formation and evolution under electric field remains lacking. Here we performed *in situ* biasing experiments in FS and conventionally sintered (CS) polycrystalline TiO_2 in a transmission electron microscope to compare the defect evolution dynamics. *In situ* TEM studies reveal the coalescence of point defects under electrical field in both FS and CS TiO_2, and subsequent formation of stacking faults, which are often referred to as Wadsley defects. Surprisingly, under the electrical field, the fault growth rate in the FS samples is 10 times as much as that in the CS TiO_2. Furthermore, the Magnéli phase, a 3D oxygen-deficient phase formed by the aggregation of Wadsley defects, is observed in the FS samples, but not in the CS samples. The present study provides new insight into defect dynamics in FS ceramics.

Key words: *in situ* TEM, flash sintering, point defects, TiO_2, Wadsley defects, defect dynamics

1. Introduction

Flash sintering has attracted significant attention given its high energy efficiency to produce dense ceramics within a few seconds or minutes [1-3]. During the flash sintering process, a moderate electrical field applied on the pre-sintered materials triggers a power-density spike on the green body when the furnace temperature ramps to the point where sample's conductivity increases dramatically. The release of high energy in a short time results in fast heating rate, accelerating the volume and grain boundary diffusion for a rapid densification process. Besides, the flash sintering technique involving quick densification and high heating rate has the capability of producing materials with defects and metastable phases. The defect redistributions have been reported in numerous oxides fabricated by the flash sintering method, such as YSZ [4, 5], TiO_2 [6], Al_2O_3 [7], Y_2O_3 [8], and $SrTiO_3$ [9].

The defect density and distribution can dramatically influence properties of ceramics. Significantly enhanced room temperature deformability was observed in YSZ and TiO_2 [10-12]. Cho et al. performed micropillar compression tests on flash-sintered (FS) YSZ at elevated temperature and observed brittle-to-ductile fracture transition at 400 ˚C, which was much lower than 800 ˚C reported in conventional bulk YSZ [11]. They ascribed the lower transition temperature to the pre-existing dislocations introduced by the flash sintering process, which accelerated the transition of deformation mode from stress-induced martensitic formation to thermally activated dislocation creep. Li et al. [12] reported 10% strain plastic deformation of FS TiO_2 without obvious cracking at room temperature via *in situ* pillar compression test in SEM, whereas conventional TiO_2 only sustained 2% strain before catastrophic fracture.

Furthermore, a strong photoluminescence phenomenon was reported in FS ZrO_2, whereas no photoluminescence phenomenon was detected in samples prepared using conventional sintering technique [13]. Yamashita et al. suggested that point defects triggered by the FS act as the photoluminescence center, exciting stable blue photoluminescence in Y_2O_3-doped ZrO_2 polycrystals. The existence of defects induced by flash sintering can lead to enhanced physical and mechanical properties and potential new applications for various ceramic systems. Therefore, the origin and distribution of defects are important factors to aid the investigation on the underlying mechanism of flash sintering and more importantly to advance the exploration on new applications of ceramics enabled by defect engineering.

In situ techniques have been considered as an effective approach to reveal the dynamic process of defect evolution. *In situ* X-ray diffraction (XRD) is used to estimate local specimen temperature and defect distribution during the flash sintering process. Lebrun *et al.* revealed an anisotropic lattice expansion in tetragonal YSZ during flash sintering, implying the nucleation of Frenkel oxygen interstitial-vacancy pairs during the flash event [14]. Charalambous *et al.* revealed asymmetrical local specimen temperature distribution and lattice distortion along specimen thickness by performing *in situ* energy dispersive X-ray

diffraction (EDXRD) on FS TiO_2 at steady state. During current holding stage, the region near anode has noticeably higher temperature and higher extent of lattice expansion compared to the rest of the specimen [15]. Further investigation on FS TiO_2 using post sintering TEM revealed that the region near anode for flash sintered TiO_2 has the highest grain size and defect density compared to the rest of the specimen, signifying the strong linkage between defect nucleation and redistribution during flash transient and current holding stage to the microstructure and defect distribution in the sintered ceramic [6, 16]. Similar phenomena have also been reported in various FS ceramic systems including CeO_2 and ZnO [17, 18].

In situ transmission electron microscopy (TEM) characterization for the defect activity under electrical bias can be used to monitor the defect formation and aggregation, directly linking the electrical properties with defect evolution, revealing underline mechanisms. This tool has been widely used in the development of memristive devices [19, 20]. For example, Kwon et al. [19] used *in situ* TEM to probe the conductivity of nanofilaments in TiO_2 thin films under electrical bias and confirmed superior conductivity of nanofilaments. Kamaladasa et al. [21] performed DC cycling sweeping experiments on single crystal TiO_2 inside TEM and reported the reversible formation of Wadsley defects and Magnéli phase, induced by the motion of positively charged point defects under bias sweeping. Most of these *in situ* bias studies focus on TiO_2 thin films with the goal to understand electrical switching mechanisms.

In this work, we applied *in situ* bias in TEM to compare the defect formation, and dynamic propagation in FS TiO_2 and conventional sintered (CS) TiO_2. In addition to trace the defect evolution kinetics, postmortem TEM analysis supported by precession electron diffraction for orientation mapping enabled us to determine the variations of grain orientations and defect nature. Wadsley defects and Magnéli phase formation have been observed in FS TiO_2. Understanding the dynamic nature of defect formation and propagation in FS ceramics is critical for the design of better processes to achieve advanced engineering ceramics.

2. Methods

2.1 Flash sintering of TiO_2

Rutile TiO_2 nanopowder with an average particle size of 50 ± 20 nm (Inframat Advanced Materials) was loaded into a 6 mm stainless steel die and compacted with a uniaxial applied pressure at 200 MPa. The height of the cylindrical green body was approximately 6 ± 0.5 mm and the green density was between 45 - 50%. Figure S1(a) and (b) show the experimental setup and sintering conditions for conventional and flash

sintering of TiO_2, respectively. For conventional sintering, the TiO_2 green body was placed in a tube furnace and heated to 1,100°C at 10°C/min. After reaching 1100°C, the temperature was held for one minute before cooling. For flash sintering, the TiO_2 green body was placed in between platinum electrodes inside a furnace. Different from sintering temperature used in CS, the sample was first heated to 900°C at a heating rate of 10°C/min. Once the temperature was reached, an electric field of 120 V/cm was applied across the sample. The combination of furnace temperature and electric field leads to current flow through the sample, which is known as the flash event. The flash event can assist sintering process of TiO_2 sample under a lower furnace temperature compared with that of CS. The current density rapidly increases to a limit set at 1.5 A/cm^2, and the power supply is switched from voltage control to current control to allow the current density to be held constant for 60 seconds. The power supply was then switched off and the samples were cooled to room temperature.

2.2 *In situ* bias testing

The TiO_2 samples were prepared using focused ion beam (FIB, Thermo Fisher Scientific Helios DualBeam) and mounted on the top of a Cu grid as Figure 1b, d shown. After a standard thinning procedure using a series of acceleration voltages of ion source to minimize the ion beam damage, the Cu grid with thin specimens were fixed on the stationary part inside the *in situ* holder (Figure 1e). The tungsten tip was mounted on the other side connected to a piezo actuator with three-dimensional movement capability. The coarse movement of the tip was executed through the high frequency vibration of piezo actuator. Changing the amplitude and frequency of the vibration can tune the moving speed of tip accordingly. The final approach was carried out by the piezo actuation when the separation distance between tip and sample is less than 1 μm.

As shown in Figure 1f, the tip was set at a negative bias and the specimen was positively biased. The *in situ* bias system shared the same ground point with the microscope system to minimize the current instability. When the tip contacted with pillars, 2 volts was set to test the connectivity. After holding at the constant voltage for a few minutes, the applied voltage was increased one volt and held. This one volt increment was repeated until applied voltage reached 7V. The dynamic defect propagation events were captured by videos accordingly.

In order to preform multiple independent *in situ* bias experiments on one TiO_2 specimen, the thin samples were cut into separated pillars as shown in figure 1f. To avoid the oxidization of tungsten tip, the tip clean procedure was performed before the *in situ* bias experiments to remove the oxide layer on the top of tungsten tip, ensuring good contact between the sample and tip.

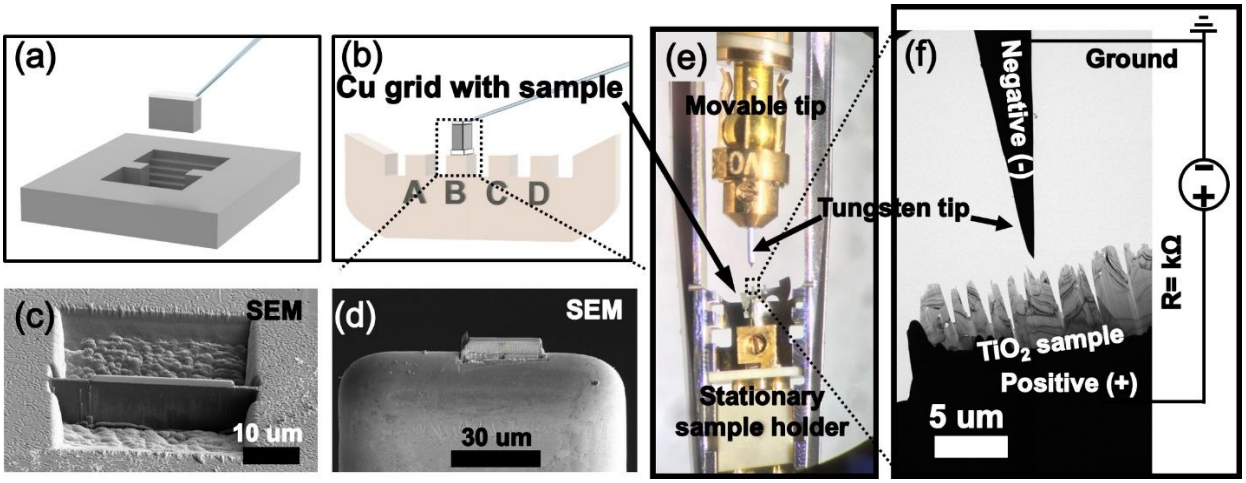

Figure 1. Schematic of the sample preparation and *in situ* bias experiment setup. (a,b) Samples were prepared by FIB and mounted on the top of Cu grid to ensure the solid mechanical and electrical contact between TiO_2 samples and Cu grids. (c,d) Corresponding SEM images of a and b. (e) The overview of *in situ* bias TEM holder. The Tungsten tip was mounted on the movable tip and Cu grid was fixed at the stationary side. (f) Low-magnification TEM image showing the setup of *in situ* bias experiment. The tungsten tip had negative voltage and the TiO_2 sample was connected to the positive side. Separated pillars were deliberately prepared to isolate the electrical influence for each test.

2.3 Microstructure characterization

Scanning electron microscopy (SEM) was carried out on a Thermo Fisher Scientific Helios G4 UX Dual Beam microscope working at 5 kV for the surface morphology characterization. The sintered TiO_2 samples were mechanically polished using diamond papers to achieve flat surface. Pt thin film was sputtered on the polished surface to avoid surface charging under electron beam. A Thermo Fisher Scientific Talos 200X Transmission Electron Microscope was used to characterize the microstructure of the as prepared and postmortem TiO_2 specimens. A specific zone axis was tilted to acquire high-resolution transmission electron microscopy (HRTEM) micrograph for defect structure analyses. The crystallography information of specimens was collected using a precession electron diffraction (PED) technique from NanoMEGAS equipped on the Thermo Fisher Scientific TALOS 200X. The precession angle and step size were 0.6˚ and 10 nm. The data was indexed using the ASTAR software package. Finally, the pole figures, orientation mapping, and grain boundary misorientation distribution were plotted using EDAX OIM V8 software.

3. Results and discussion

Figure 2a shows the surface morphology and grain size of conventional sintered TiO_2. A TEM micrograph of *in-situ* specimen prepared from the CS sample (Figure 2b) shows the microstructure from a cross section view. Pillars were deliberately prepared to isolate the electrical and thermal interference from each test. Different from the CS TiO_2 sample, voids were identified along grain boundaries (GBs) sporadically in FS sample shown in figure 2 (d,e). figure 2(c, f) show the GB misorientation angle between two adjacent crystals for the areas marked in figure 2(b, e) and the corresponding color code is listed at the bottom of the figures. Most GBs were high angle GBs, which are marked in blue and green colours. Twin boundaries, marked by the yellow color, were also spotted occasionally both in CS and FS TiO_2 specimens. Crystallographic information of as-prepared CS and FS TiO_2 specimens are present in figure S2. Pole figures show a random texture distribution of grains for both specimens, revealing the polycrystalline nature of TiO_2 samples fabricated by both CS and FS methods. Figure S2b shows the GB misorientation distributions of CS and FS samples. Except a minor discrepancy in low angle GBs and 60˚ misoriented GBs, two distributions share a common trend and correlate well with the standard distribution of polycrystalline materials.

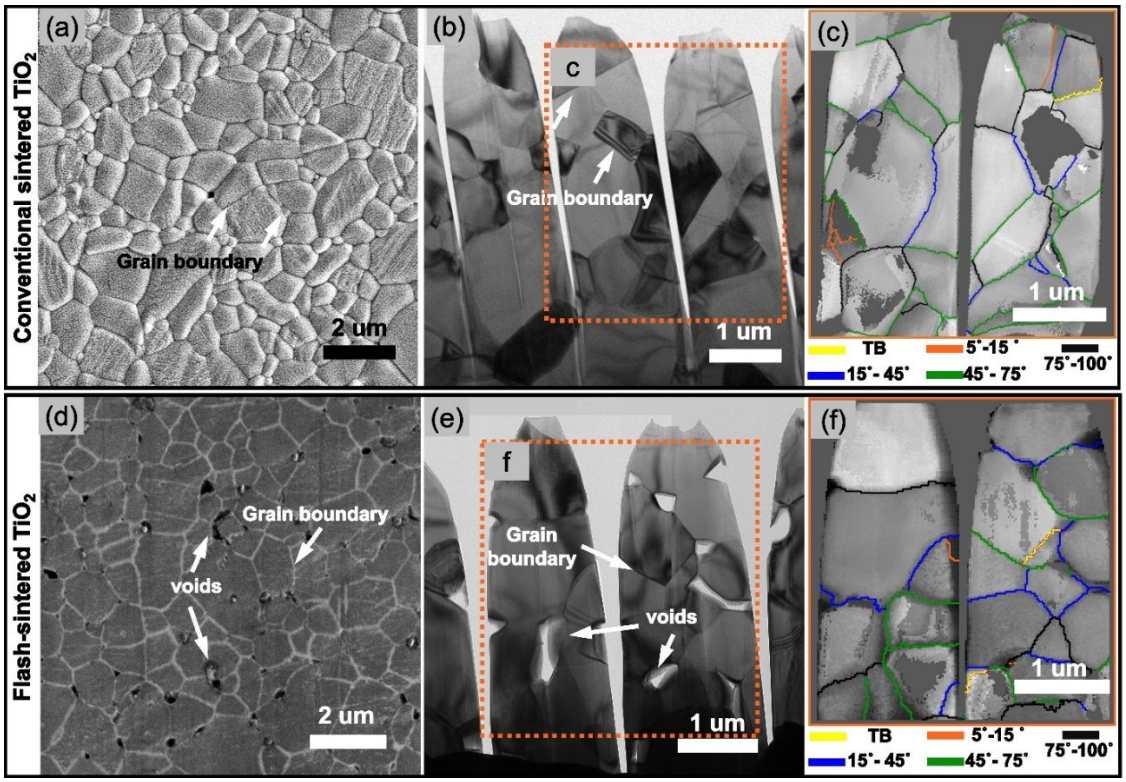

Figure 2 Microstructure characterization of conventional-sintered (CS) and flash-sintered (FS) TiO_2. (a,d) SEM micrographs show the similar grain size between two samples and a higher porosity in the FS TiO_2. (b, e) TEM micrographs of CS and FS TiO_2. (c,f) ASTAR grain boundary (GB) maps illustrate the grain misorientation angles in both samples. Yellow line indicates the location of twin boundaries (TBs).

3.1 Nature of defects in TiO_2 induced by electrical bias

Defects have been observed in high temperature annealed TiO_2 bulk samples [22]. Under vacuum or reducing agents, oxygen anions can migrate to surface and transform to gas phase or interact with reductive gas due to lower oxygen potential on the surface, resulting in oxygen deficiency in TiO_2 sample. The defect evolution and formation mechanisms have been thoroughly studied by Bursill et al. [23] in oxygen deficient bulk TiO_2. In general, point defects, dislocations, planar defects, and 3D new phases were observed in nonstoichiometric TiO_2 and defect formation in titanium dioxide are closely related to the oxygen deficiency level. A hypothetical oxygen nonstoichiometry number x in form of TiO_{2-x} is used to quantify the level of oxygen deficiency. When x is less than 0.0001, randomly distributed point defects were observed in TiO_{2-x} [22]. It has been reported that the maximum x for TiO_{2-x} is on the order of 10^{-4} to accommodate statistically distributed point defects (oxygen vacancies) [24]. When x is greater than 0.0001, a high point-defect concentration triggers the formation of planar defects named as Wadsley defect due to the aggregation of point defects, which was first identified by Wadsley in niobium oxides [25]. If x exceeds 0.001, defects aggregated to form new structure and TiO_{2-x} cannot be considered as a defective rutile TiO_2. Instead, Magnéli phase forms due to periodic arrangement of Wadsley defect.

In addition to the thermal activation, electrical bias can facilitate defect formation in TiO_2. The applied electrical field triggers electrochemical reduction of TiO_2 via oxygen ionization. The point defects including oxygen vacancies and Ti interstitials move under the electrical field to the cathode [26, 27]. Postmortem TEM micrographs were acquired for FS and CS TiO_2 specimens after *in situ* bias experiments. A dark contrast region was observed in FS TiO_2 sample shown in figure 3a. A diffraction pattern from area b in figure 3a was acquired along [111] zone axis. Besides the normal diffraction spots from various planes like $(\bar{1}01)$ and $(\bar{1}10)$ planes, two abnormal phenomena were spotted in figure 3b. First, obvious streaks around diffraction spots indicate the formation of planar defects, which marked by yellow dash line. In TiO_2, the streak of diffraction spots is considered as the signature of Wadsley defect [20, 22, 28]. Second, superlattice spots along $(\bar{1}01)$ planes suggest a new periodic structure formed during *in situ* biased experiments. Bursill et al. revealed the correlation between Magnéli phases and superlattice spots from corresponding diffraction patterns [23]. In general, the superlattice spots indicate the formation of Magnéli phase, and Magnéli phases with different oxygen reduction levels have different separation distance in superlattice spots. Kamaladasa et al. also reported similar types of superlattice spots as the evidence of $Ti_{17}O_{33}$ Magnéli phase [20]. Thus, the superlattice spots in figure 3b marked by red circles suggest the formation of Magnéli phase in area b triggered by the electric field. Zig-zag Wadsley defects are shown in figure 3c with discontinuous segments. Figure 3d shows defect morphology in box d of figure 3a, which is close to the defect propagation frontline. High-density segments aggregated along both $(\bar{2}11)$ and $(\bar{1}2\bar{1})$

planes. Different from stress contour or other artifacts, the dark contrast contained high-density Wadsley defects with various morphology. A clear interface or boundary can be identified between Wadsley defects and matrix from enlarged view. Figure S3 shows the stress contour and Wadsley defects in the same sample. The stress contour moved when tungsten tip bended the specimen, whereas the Wadsley defects only propagated under electrical bias.

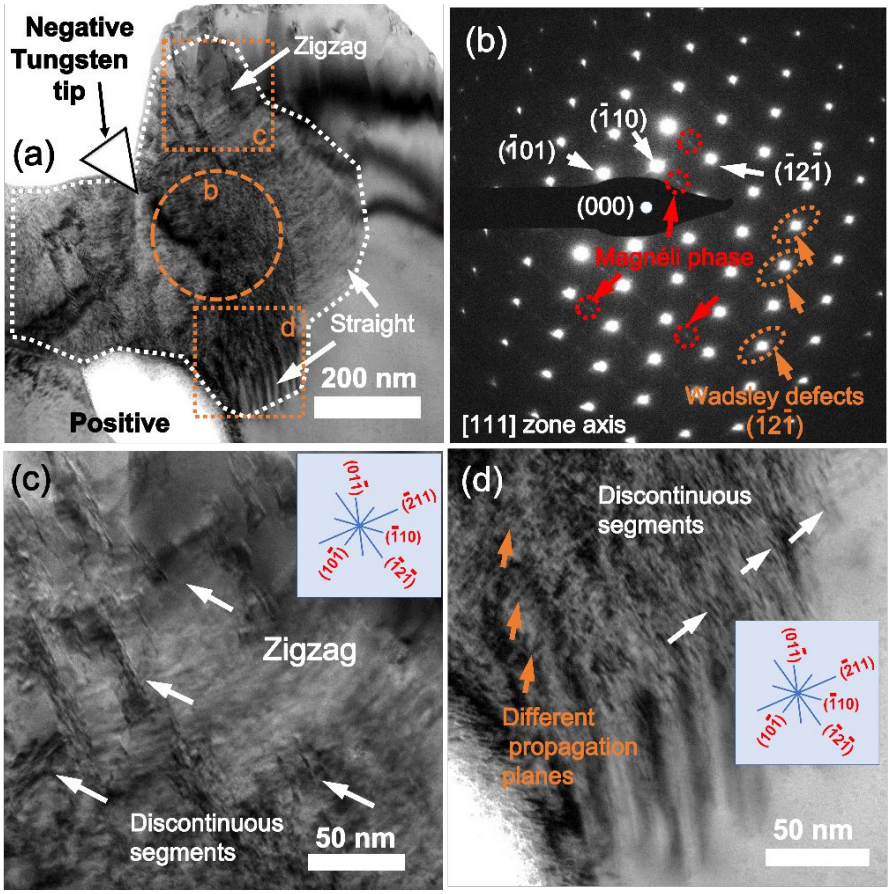

Figure 3 Post-mortem TEM micrographs of the FS TiO_2 sample. (a) Bright field TEM micrograph shows the formation of Wadsley defects and Magnéli phase after a quasi-DC bias test. The negative bias was applied to the tungsten tip touching the top portion of the sample. (b) Diffraction pattern acquired from [111] zone axis for box c in Fig. 5a shows the existence of Wadsley defects and Magneli phase. (c, d) Representative defects morphology formed under electrical bias. The defects propagated along different crystal planes.

A dark field TEM micrograph of CS TiO_2 (Figure 4a) clearly shows the existence of high-density defects with white contrast. The defects exhibited various morphologies inside one grain, suggesting different aggregation planes under electrical field. Figure 4b shows the diffraction pattern with streaks, suggesting the formation of Wadsley defects. Different from Wadsley defects observed in high-temperature-annealed TiO_2 sample with homogenous and continuous band structure [22], the majority of defects were small discontinues segments and aligned along the current flow direction. Figure 4c shows

two typical defect morphologies, the zig-zag shape and straight-line shape in the CS sample. The zig-zag defects extended along orthogonal direction, implying that the defect may change the propagation planes under electrical bias. Compared with the zig-zag defects, straight-line defects were the dominant morphology and away from the tip-sample contact point. These segments were all parallel to each other and aggregated along the electric field direction. Figure 4d (a magnified micrograph of area d in figure 4a) shows straight-line segments with various thickness, or band width. The narrow line defects were marked by orange arrows, whereas white arrows point out the defects with a few nanometers width. The discrepancy of the defect width may result from the different propagation planes shown similarly in figure 3c, 3d. For the narrow line defects, the aggregation planes were parallel to the view direction, while the propagation planes of thicker straight-line defects were inclined to the incident beam.

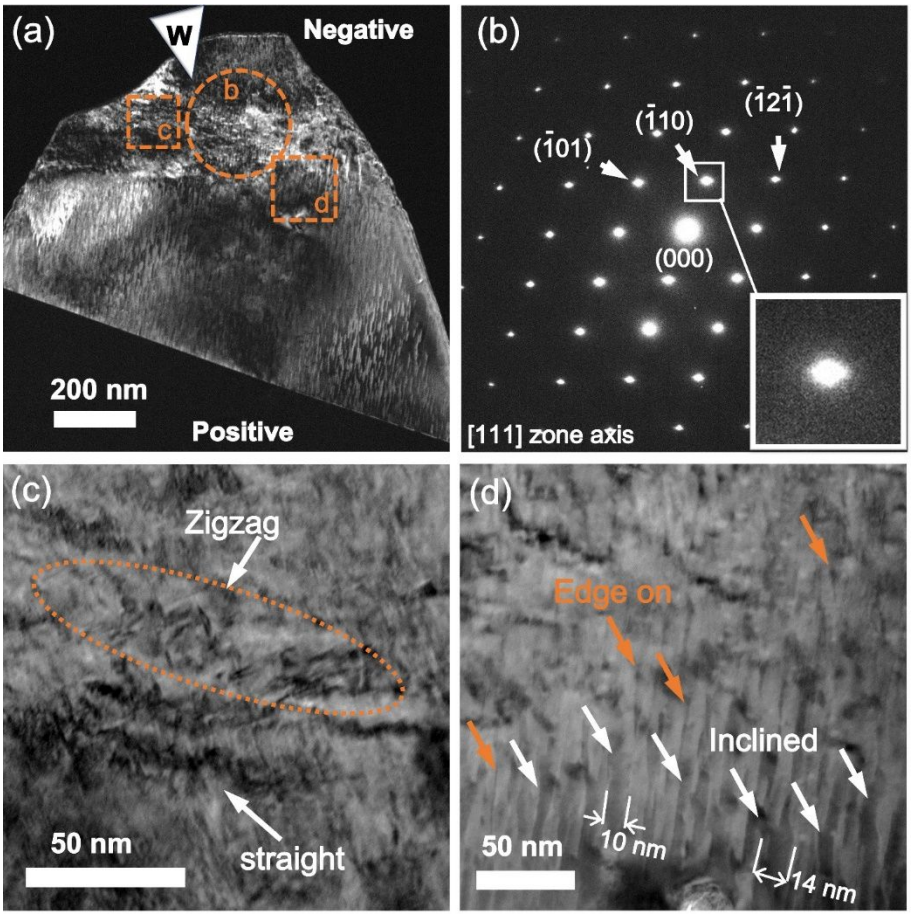

Figure 4 Post-mortem TEM micrographs of the CS TiO_2 sample. (a) Dark field (DF) TEM micrograph shows the formation of Wadsley defects after electrical bias. (b) Diffraction pattern acquired from [111] zone axis for area b in Fig. 6a. (c, d) Representative defect morphology formed under electrical bias.

3.2 The formation mechanism of Wadsley defect

A general Wadsley defect formation mechanism has been under debate due to the complexity of defect formation process including nucleation, aggregation, and swing in various transition metal oxide systems. Although several models can explain specific cases, there is still no general mechanism that fits for all systems. A dislocation expansion mechanism was proposed by Anderson and Hyde [29], which shares similarity with the formation of intrinsic stacking faults in metals. Under high temperature and low oxygen partial pressure, oxygen atoms close to the surface are prone to transform into gas phase, leaving oxygen vacancies inside the crystal. The vacancies aggregate into discs or column along specific crystal planes at low vacancy concentrations, the process was also reported in $SrTiO_3$ [30]. With the increase of vacancy concentration, discs connect and form two dimensional Wadsley defects, one type of planar faults. Wadsley defect expands by the climb of the bounding dislocations due to the attraction force of the dislocation for the surrounding anion vacancies. Since surface has the lowest oxygen potential, Wadsley defect nucleates close to the sample surface and expands to the crystal interior. On the contrary, a cooperative diffusion mechanism was proposed by Andersson and Wadsley, which solely depends on the cation migration [25]. On the sample surface, the titanium potential drives the Ti atoms to diffuse cooperatively from the surface into the subsurface or deeper interior. Ti cations hop from original crystal position to an interstitial site forming extrinsic planar defects and corresponding oxygen atoms transform into gas phase.

Similar oxygen vacancy/titanium interstitial domination debate exists for the formation of Wadsley defects triggered by electrical field. Under electrical bias, the electrochemical redox process creates oxygen vacancies in oxides, releasing two electrons to the conduction band to increase the conductivity [31, 32]. Since oxygen vacancies in many oxide systems act as mobile donors [33-36], substantial experiments have been performed to study electrical properties and corresponding defect migration dynamics in functional oxides based on the oxygen-migration model. Kwon et al. [28] performed *in situ* TEM bias experiment on single crystal TiO_2 and observed Wadsley defects close to the cathode. The formation of Wadsley defects was ascribed to the coalescence of oxygen vacancies migrating under electrical field and aggregating close to the negatively biased electrode. Similar phenomenon was also reported by Kamaladasa et al. [20] for TiO_2 single crystals. However, under the condition of low oxygen activities, Ti interstitials have been proved to dominate the point-defect equilibria [37-39]. Furthermore, different from many perovskites that contain immobile cation interstitials, Ti interstitials and O vacancies both have high mobility in reduced rutile phase [40, 41]. Based on the transition-state theory calculations, along <001> and <110> directions, Ti interstitials have lower migration energy than O vacancies [42]. Moballegh et al. studied the electric-field-induced point defect distribution in reduced TiO_2 and reported a high-density point defect (both O vacancies and Ti interstitials) region close to the cathode. At a low electric-field, in absence of abrupt filamentary event, a

drift-diffusion based homogeneous defects migration was identified and Ti interstitials dominate as confirmed by postmortem EELS analysis close to the cathode region [27].

Postmortem HRTEM micrographs acquired from [111] zone axis show the co-existence of extrinsic and intrinsic planar defects in FS TiO_2 specimen in figure 5a. In general, the planar stacking fault is formed by either removing or inserting an atomic layer, which also are named as intrinsic or extrinsic faults. For TiO_2, the aggregation of oxygen vacancy results in the missing of oxygen layer, suggesting the formation of intrinsic fault. On the contrary, the Ti interstitial precipitation would insert atomic layer, indicating the extrinsic nature of the planar defects. Therefore, the co-existence of two types of planar defects reveals the cooperative dynamic process of oxygen vacancy and titanium interstitial under electrical field. Inverse FFT was carried out for $(\bar{1}2\bar{1})$ and $(01\bar{1})$ in figure 5b and figure S4. In figure 5b, for $(\bar{1}2\bar{1})$ planer defects, both intrinsic (marked by orange dash circles) and extrinsic (indicated by orange dash rectangles) defects were observed after bias experiments. The length of Wadsley defects is a few nanometers, quite different from the continuous and homogeneous Wadsley defects in annealed TiO_2 samples. The IFFT was also conducted on Postmortem HRTEM micrographs of CS TiO_2 shown in figure 5d and figure S5. $(\bar{1}2\bar{1})$ intrinsic and extrinsic planar defects were also identified.

More experimental evidence implies that the defect formation involves the activity from both titanium interstitial and oxygen vacancy [43-45]. Hasiguti reported the existence of Ti interstitial pair around the oxygen vacancy clusters in slightly reduced TiO_2. They observed the drop of Ti interstitial density during the formation of new planar defects in TiO_2 sample by means of electron paramagnetic resonance (EPR) since all defects have signature peaks in the EPR spectra [43], suggesting the contribution of Ti interstitials on the formation of planar defects. By tuning the oxygen deficiency level of TiO_2, Aono et al. found that Ti interstitials aggregated along {121} cooperated with the oxygen vacancies, assisting the formation of {121} planar defects [46]. Bursill et al. [44] identified the extrinsic planar defects in TiO_{2-x} and intrinsic planar defects in WO_{3-x}. They suggested that the extrinsic or intrinsic nature of planar defects may lead to the relatively high concentrations of one-dimensional defects during the defect precipitation.

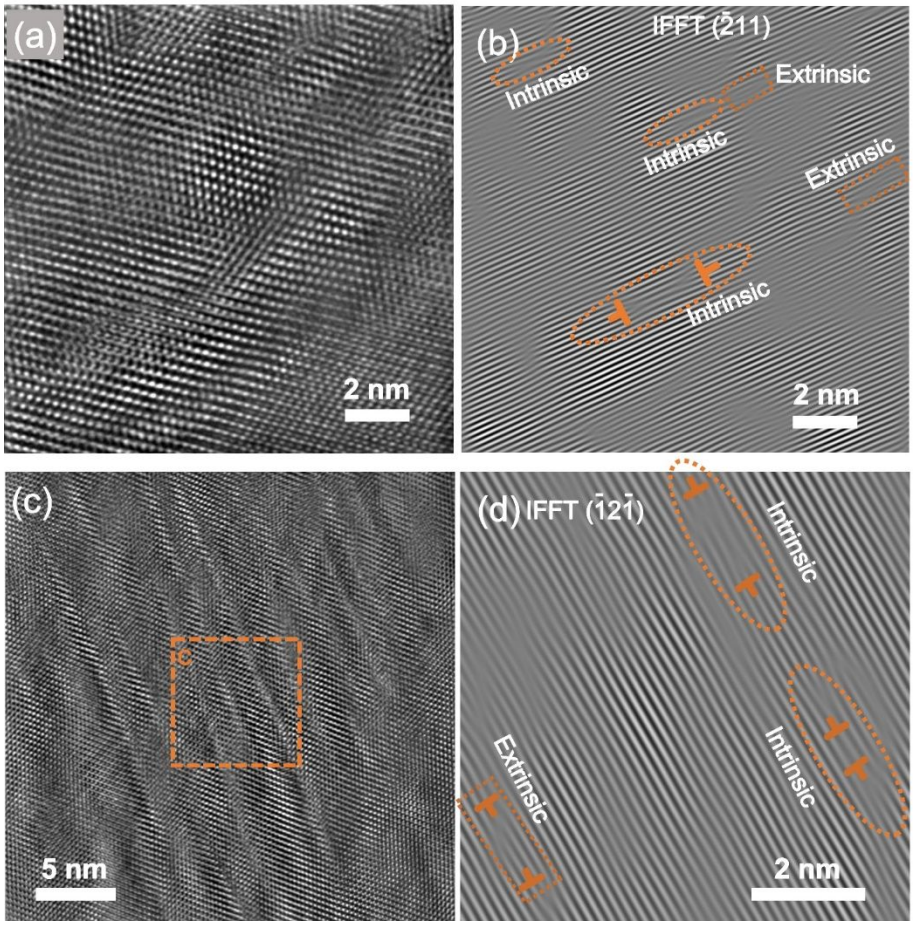

Figure 5 Postmortem HRTEM micrograph of the FS and CS TiO_2 showing the extrinsic and intrinsic nature of planar defects. (a,b) HRTEM and corresponding IFFT micrographs showing (the extrinsic and intrinsic) Wadsley defects formed under bias in the FS TiO_2. (c,d) HRTEM and IFFT images showing similar defects formed under bias in the CS TiO_2.

3.3 The propagation of Wadsley defect

Two distinct Wadsley defect propagation mechanisms were identified during the *in situ* bias experiments for both CS and FS samples. Once the voltage rose to 4V, in one second, a dark contrast close to the cathode emerged (figure 6b) in the CS TiO_2. The dark area triggered by filamentary event consist of small segments of planar defect shown in figure 4c and 4d. In-depth studies have been carried out in thermal induced Wadsely defects via *in situ* TEM heating experiments. Blanchin et al. [47] studied the planar defects dissolution and precipitation, suggesting a strong dependence of planar defect growth rate both on local cooling rate and on the initial defect concentrations. Millot et al. identified the correlation between the cooling rate and the morphology of planar defects [48]. Homogeneous and continuous planar defects form under low cooling rate, whereas fast cooling rate results in less ordered and segmented planar defects. Besides the morphology discrepancy between the bias induced and thermal induced bulk TiO_2 samples, the

propagation process of Wadsley defect also varies. In high temperature annealed sample, the aggregation planes were closely related to the oxygen deficiency level. Wadsley defects were observed propagating along {121} planes in the high temperature annealed TiO_2 [29]. Bursill et al. identified propagation planes other than {121} planes in reduced TiO_2 [22]. In slightly-reduced rutile ($TiO_{1.995}$), Wadsley defects nucleate along {132} and {101} family planes. With the increase of oxygen deficiency level (TiO_x when $1.75 \leq x \leq 1.889$), propagation planes switch to {121} and {101} planes, which are more closely packed planes. Contrarily, various morphologies of Wadsley defects indicate defects propagated on different planes during the filamentary event, suggesting that energy spike excited defects aggregation along different crystal planes simultaneously.

The 4 V in our experiments is the threshold voltage for the charge carrier avalanches. This threshold voltage was also referred to the dielectric breakdown voltage, transforming the insulator to conductive material. Since the dielectric breakdown stimulates the formation of filaments as the conductive path, the breakdown voltage is also named as filamentary switching voltage [49]. When the applied voltage is lower than the filamentary voltage, where the local change in ionic concentrations is too small to affect the conductivity, defects follow a 1D drift-diffusion mechanism and obtain a stable state without obvious concentration change across the oxides [49]. Gradual increment of applied voltage below filamentary voltage causes the accumulation of point defects accompanied by a gradual decrease of sample resistance without detectable Wadslely defect formation [20]. In our experiments, when the applied voltage was below 4V, the current was less than 1 uA. There is no observable Wadsley defect formation event captured below the filamentary switching voltage for specimens. On the contrary, defect concentration surges significantly near the cathode when applied voltage exceeds filamentary point. Wadsley or Magnéli defects form abruptly followed by resistance drop [20].

Once the applied voltage exceeded the breakdown voltage (4V in the current experiments), the increase of applied voltage can initiate new filamentary event adjacent to previous filament region within one second, extending the growth and density of filaments along current flow direction in CS TiO_2 (Figure S6). Filamentary event was also identified in the FS sample when the applied voltage exceeded 4V as shown in figure 6e, 6f. Figure 6e shows the bias induced a new filamentary event when the applied voltage elevated from 4V to 5V. When the voltage rose to 6V, another filamentary event occurred along the applied field direction close to pre-existing filaments shown in figure 6f. The abrupt filamentary activities have been observed in both the CS and FS specimens, while the FS specimen have a larger filamented area than that in the CS specimen, resulting from a higher defect density in FS specimens.

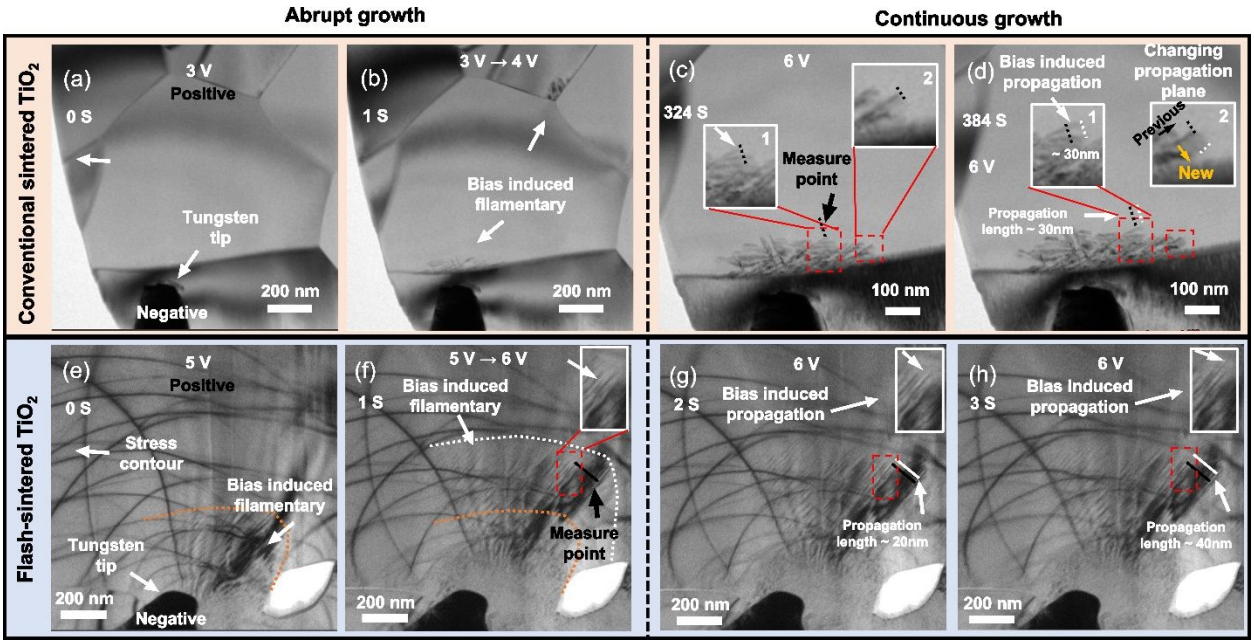

Figure 6 Two types of defect formation mechanisms under bias for TiO_2. (a, b) TEM snapshots showing the abrupt filamentary nucleation and growth when applied DC voltage increased from 3V to 4V for the CS TiO_2. In 1 s, dark cloud emerged from the GBs indicated by the arrows. (c, d) TEM snapshots of CS TiO_2 show the filaments propagated continuously under 6V bias after the abrupt nucleation. The defect marked by an arrow in the magnified image 1 gradually grew by 30 nm in 60 s. Another defect in the enlarged box 2 propagated onto another plane under 6V. (e, f) In the FS TiO_2, when the voltage rose from 5 to 6V in 1 s, numerous filaments formed between the yellow and white dotted lines in 1 s in Fig 8f. (g, h) At 6V, filaments in the FS TiO_2 extended along the same direction by 20 nm in 1 s.

Besides the abrupt filament formation event, a distinct continuous filament propagation phenomenon was also observed in both the CS and FS TiO_2 during the constant voltage holding period at higher voltage (> 5V). At 6V, the filaments in CS TiO_2 continuously propagated along the current flow direction during the voltage holding period as shown in figure 6c, d. The filament in enlarged image 1 in figure 6c moved forward 30 nm in 60 s. Another propagating filament enlarged in box 2 in figure 6c deviated from the original plane. More continuous-defect-propagation events were captured in our experiments.

Figure 7 shows snapshots of defect propagation events in FS TiO_2 specimen under the electrical field at 6 volts. Snapshots show continuous defect propagation under a constant electrical field. At 7 second, the defect marked by the yellow circle initiated and propagated from negative side to the positive side. After 1s, the defect moved rightward 16 nm and another defect that paralleled to the original one emerged. The defect kept expanding along the same direction and exceed 30 nm in 2s (see the corresponding videos in the supplementary material).

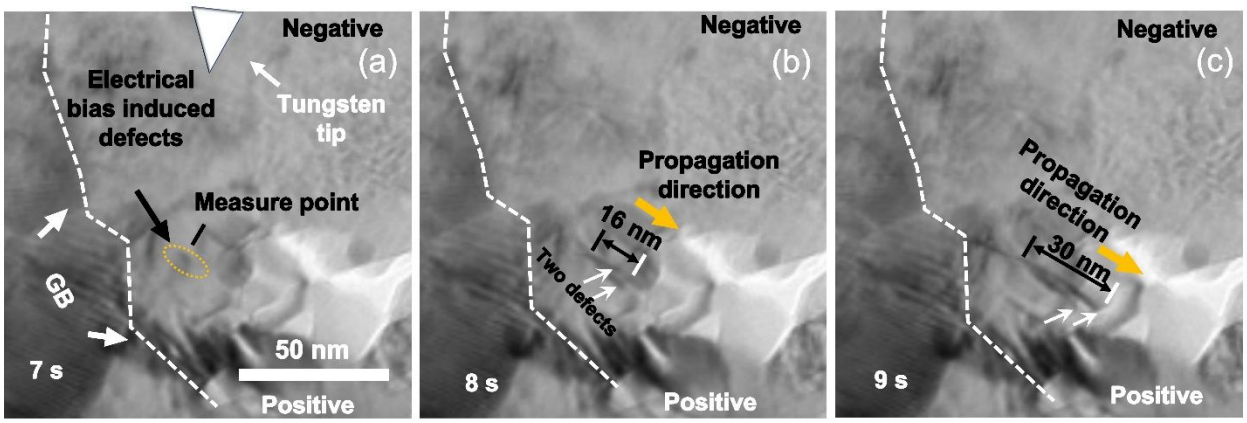

Figure 7 Snapshots showing defect propagation under constant electrical field in the FS TiO_2. The tungsten tip was in contact with the top of the sample. (a) Defect propagation under 6V DC bias. (b) In 1 s, two defects formed along different planes and propagated over 16 nm. (c) Defect propagation along the opposite direction. Yellow arrows point out the defect propagation direction.

The comparable *in situ* bias experiment was also performed on CS samples. The contact point of tungsten tip is marked by the white arrow at the top of figure 8a. When the voltage increased from 4V to 6V, an abrupt filamentary formation event took place in one second shown over a large area with dark contrast in figure 6a. It is interesting to note distinct defect morphology in different grains. Top grain contains defects aligned with the electrical field, whereas the defects in the bottom grain propagated toward the right of the sample, presumably influenced by the grain orientation. During the voltage holding period, 120 s at 6 V, the filaments started to propagate towards the anode (downward) gradually. Figure 8a shows the onset of continuous defect propagation at 6 V after the abrupt filament generation. After 60 s, the frontline of defects moved forward to the anode side by 37 nm (figure 8b). After 120 s, the accumulative propagation distance of the stacking faults reached 61 nm (see the corresponding videos in the supplementary material).

Figure 9 shows the statistics of aggregation velocity from the multiple Wadsley defect propagation events captured during *in situ* bias experiments. The average propagation speed of Wadsley defect in the FS specimen is about 10 nm/s, whereas the Wadsley defect growing speed is about 1 nm/s in CS specimen. The velocity deviation for both FS and CS specimens may result from the local orientation, electrical field, and the grain boundaries. Although different sintering methods with various calcination temperature may lead to distinct grain size distribution in specimens, the grain regions with very similar grain size both in FS and CS samples were observed and selected to prepare micro scale in-situ samples to mitigate the influence from grain size deviation. The low bound of propagation speed for FS is 7 nm/s, which much higher than the upper bound of propagation speed for CS sample (1.3nm/s), suggesting a significant difference of defect growing rate between FS and CS samples. Since Wadsley defects are bounded by partial dislocations, the climb of partial dislocations via absorbing adjacent point defects facilitates the expansion

of Wadsley defect [10]. Thus, a higher growth speed indicates shorter point defect migration time to the front of Wadsley defect, the core of partial dislocations. Both global point defect density and point defect velocity contribute to the Wadsley defect propagation speed. In our experiments, same voltage (6V) was applied on FS and CS specimens with similar current (0.02-0.03mA) after filamentary. Therefore, the global point defect density might be the dominant factor to control the Wadsley defect propagation. Meanwhile, the new sample fabrication technic, flash sintering method, generates high temperature spike, and introduces high-density point defects under electric field [12]. Hence, the high-density point defects in FS specimen could be the leading factor for the high propagation speed of the Wadsley defects.

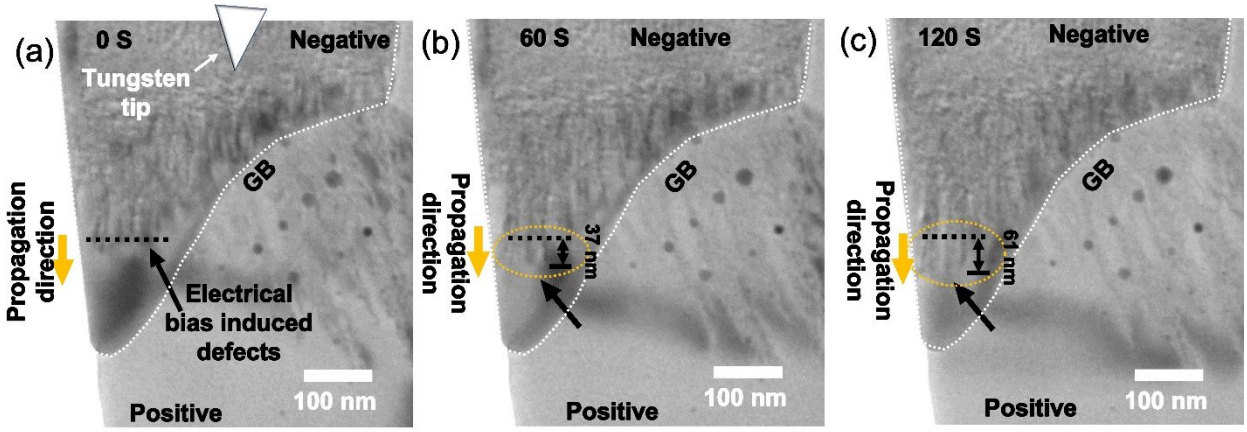

Figure 8 TEM snapshots showing defect propagation under constant electrical filed for the CS TiO_2. The tungsten tip was in contact with the top of the sample as marked by white triangle. (a) The dark feature indicated the formation of defects under electrical field. The black dash line shows the starting point of defect propagation when the applied voltages was 6 V. (b) In 60 s, multiple defects propagated towards the positive side by 37 nm. (d) By 120 s, the propagation distance reached 61 nm.

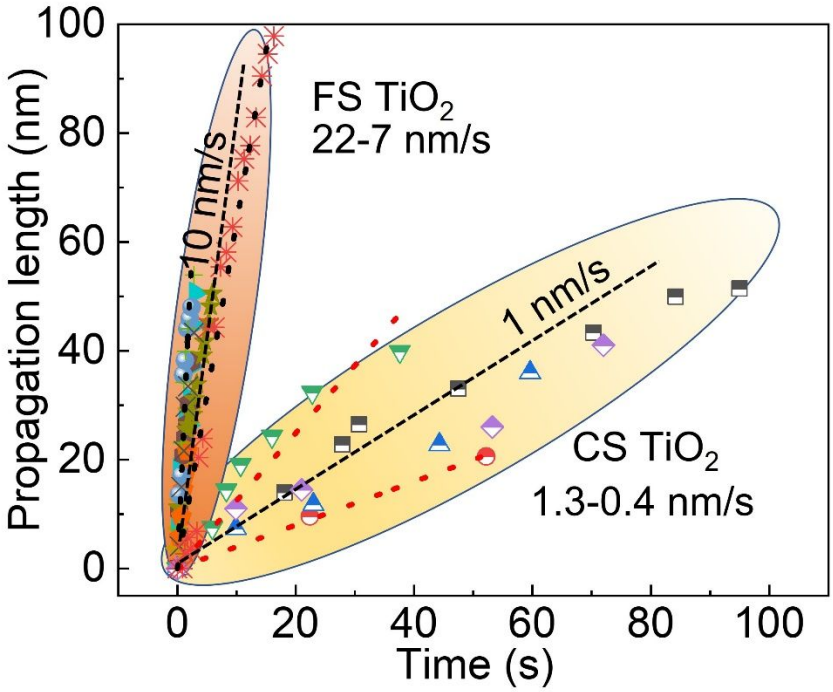

Figure 9. Comparison of defect propagation length vs. time under 6V DC electrical bias for CS and FS TiO_2. The average defect propagation rate in the FS TiO_2 is 10 nm/s, comparing to 1 nm/s in the CS TiO_2.

3.4 The formation of Magnéli phase in FS TiO_2

The Magnéli phase can be considered as periodic stacking of planar defects along specific planes in substoichiometric TiO_2 with a general formula Ti_nO_{2n-1}. A smaller spacing indicates higher Ti atomic ratio. In general, Ti_4O_7, Ti_5O_9, Ti_8O_{15} were frequently observed in Magnéli phases [26, 50-52]. Bursill et al. [22] studied microstructure of slightly recued rutile and summarized the relationship between Ti/O ratios and planar defects spacing along different aggregation planes ({121}, {132}, {101}). They revealed a clear trend for Magnéli phase evolution with the increase of oxygen deficiency level. Moreover, in annealed substoichiometric titanium dioxide, various planar defect spacings were identified in the same specimen, indicating the coexistence of multiple Magnéli phases [26].

However, the formation mechanism of Magnéli phase under electrical field remains unclear. Kwon et al.[19] performed electrical bias experiment on 40-nm-thick TiO_2 and suggested Magnéli phase formed directly during filamentary event. HRTEM analysis discovered multiple Ti_4O_7 nanoscale filaments across the film with 0.1 to 5 μm separation distance. Kwon et al. [19] carried out *in situ* TEM bias experiments on single crystal TiO_2 with quasi-DC voltage sweeping from 0 to -1.1V. Only {121} Wadsley defects emerged on the cathode and aggregated towards the anode side. Under similar experimental setup, Kamaladasa et al. [20] observed the Magnéli phase after 52 cycles of DC sweeping in TiO_2. Based on the evolution of diffraction pattern captured after each DC sweeping cycle, Wadsley defects gradually transformed to Magnéli phase with accumulated DC sweeping cycles.

Even for the same specimen, defect propagation and Magnéli phase formation are affected by various factors. First, the sample dimension and applied voltage control the dissipated power density that is related to the driving force for point defect formation and aggregation. Besides, higher dissipated power may be associated with extensive local Joule heating that can trigger high temperature (>1500 ˚C) close to the cathode position, stimulating the defect migration and facilitating Magnéli phase formation. In Kwon's case, the current flow restricted in a few nanometers narrow filaments generated more than 20 mW and may heat the local area up to 3000 ˚C [19, 53]. Second, point defects diffusion activity is sensitive to the crystal orientation since all Wadsely and Magnéli phases have certain propagation planes. Last, from a technical point of view, the diffraction patterns that are used as primary evidence for the formation of Wadsley and Magnéli phase require specific zone axis to show the features like streaking lines or superlattice spots. For example, if the incident beam is parallel to [100] zone axis, theoretically it is impossible to observe diffraction spots from {132} planes.

In our experiments, FS and CS TiO_2 pillars with similar geometry and crystal orientation were chose and were applied under the same voltage. We compared defect morphology in FS and CS specimens with similar zone axis (Figure 10a, e) after bias. Figure 10b shows the postmortem dark field TEM

morphology of CS specimen and the corresponding diffraction pattern of area c captured along [010] zone (Figure 10c). The streaks of diffraction spots marked by orange dash circles indicate the formation of Wadsley defects. The diffraction pattern of area d shows round spots (figure 10d), suggesting a low Wadsley defect density and less crystal distortion away from area c in which Wadsley defects were spotted. In contrast, the diffraction pattern of area g in FS specimen shows the satellite spots along $(10\bar{1})$ and $(\bar{1}0\bar{1})$ planes, suggesting the formation of Magnéli phase after the filamentary event. Away from the area g, close to the edge of the dark cloud in figure 10f, the diffraction pattern of area h shows the streaks, revealing the formation of Wadsley defects (Figure 10h). Under similar current history and observation condition for both the CS and FS specimens, Magnéli phase formed in the FS specimen, whereas only Wadsley defects were detected in the CS specimen. Since pristine FS specimen has a higher point defect density than that in the CS specimen, the pre-existing defect density may play an important role on Magnéli phase formation.

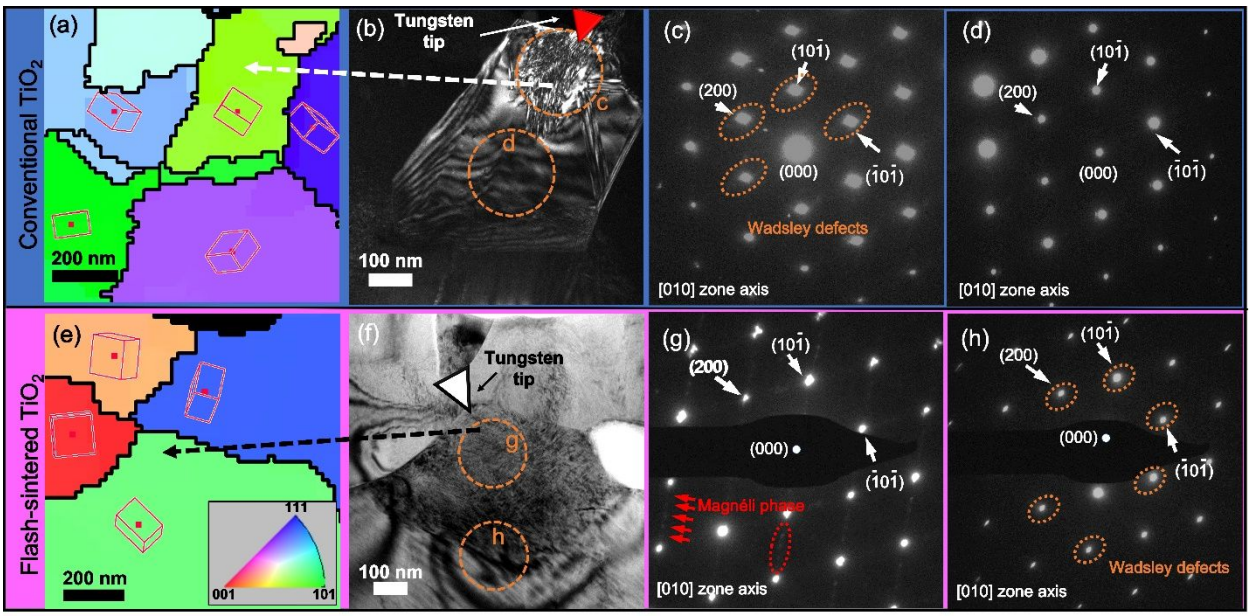

Figure 10. The comparison of defect formation during *in situ* bias experiments between CS and FS TiO_2 with similar geometry, crystal orientation, and electrical bias history. (a,e) Orientation map of the two samples, the surface normal of samples in the maps are rendered by orientation color key inserted in b. (b) Post-mortem DF TEM micrograph of CS TiO_2. (c) The diffraction pattern from circle c in Fig. 10b shows the formation of Wadsley defects. (d) the diffraction pattern from circle d outside the defect zone for comparison. (f) Post-mortem TEM micrograph of FS TiO_2. (g) The diffraction pattern from circle g in Fig. 10f shows the formation of Wadsley defects and Magnéli phase. (h) The diffraction pattern from circle h at the edge of defect zone shows the formation of Wadsley defects.

As mentioned earlier, the Magnéli phases are substoichiometric TiO_2 with various periodic Wadsley defect stacking. Thus, the density of Wadsley defects dominates the formation and the evolution of Magnéli phases. Moreover, the density of Wadsley defects is governed by point defect density generated either by

the flash sintering or applied external field during the *in situ* bias experiments. Thus, the point defects govern the Wadsley defects and Magnéli phase formation. Previous study also shows a higher point defect density in FS samples than that in CS samples, which also attributes to the superior mechanical properties of TiO_2 [12]. Magnéli phase formation mechanism is shown schematically in figure 11. Under a higher point defect density, multiple planar defects nuclear from the point defects aggregation and extended along same crystal plane in a periodic manner, forming the Magnéli phases. If point defect density is low (Figure 11c for the CS TiO_2), less planar defects form due to the large separation distance of point defects. Thus, there is no detectable Magnéli phase in the CS sample. Only enough accumulation of defect can trigger the formation of Magnéli phase, like the Magnéli phase formation after multiple bias sweeping preformed in Kamaladasa's work [20]. For flash sinter method, there are three major routes that can be utilized to promote the Magnéli phase formation. First, the increase of steady state current limit during the flash sintering can trigger the Magneli phase formation. Second, instead of applied bias once temperature reached 900°C, increase holding time at 900°C for a few minutes before applying bias also promote the Magnéli phase formation. Last, by conducting a second DC flash sintering with the reversed polarity, one can effectively concentrate the oxygen vacancies within the specimen into the region near the original positive electrode making it much reduced with high density planar faults/ crystallographic shear planes. In general, an oxygen deficiency environment needs to be secured such as high vacuum condition during in-situ experiments in TEM. In some cases, hydrogen atmosphere and high temperature can be applied to expedite oxygen reduction process which facilitate the phase transformation from rutile TiO_2 to Magnéli phase [6, 15-16, 54-55].

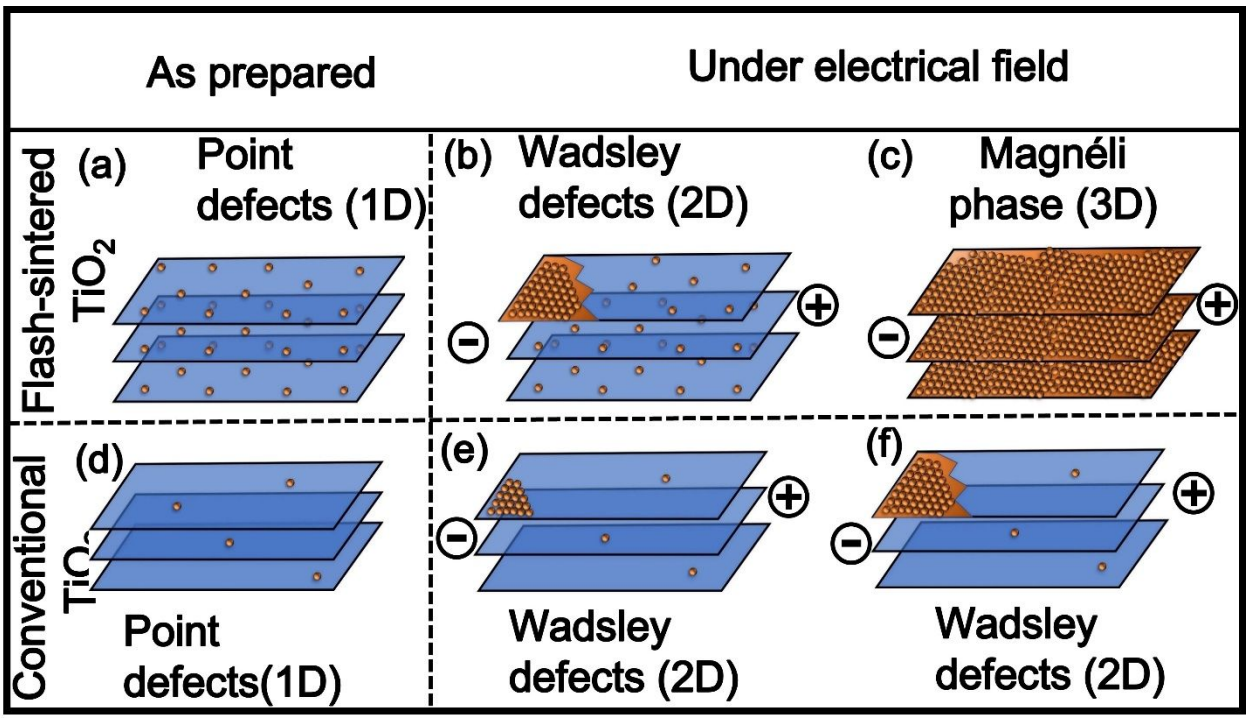

Figure 11. A schematic illustration on the difference of defect formation between CS and FS TiO_2. (a,d) The as-prepared FS TiO_2 has high-density oxygen vacancy introduced during the flash sintering. (b,e) Under electrical bias, the pre-existing defects with positive charge move towards negative electrode and aggregate to form Wadsley defect clusters. In CS TiO_2, the Wadsley defect formation rate is low due to the low-density pre-existing point defects. (c,f) The high-density pre-existing point defects promote the formation of Wadsley defects, which accumulate to nucleate the Magnéli phase. The FS TiO_2 has much greater fraction of Magnéli phase evolving from the Wadsley defects.

4. Conclusion

In situ bias experiment was performed on FS and CS TiO_2 polycrystalline samples inside a transmission electron microscope. The intrinsic and extrinsic planar defects (Wadsley defects) were identified in both specimens, suggesting the contribution from both Ti interstitials and oxygen vacancies under the electrical field. Different from the homogenous and continuous defect formation in thermally annealed TiO_2 sample, small segments of Wadsley defects were identified as the dominant features due to the nonequilibrium fast defect formation process. An order of magnitude higher Wadsley defect propagation speed was observed in the FS TiO_2 compared to that in the CS TiO_2. The major differences in the defect propagation speed may result from the different build-in point defect density in the specimens. Moreover, high-density point defects in the FS TiO_2 also facilitated the formation of Magnéli phase. Our

in situ experiments suggest the vital role of point defects on the formation and dynamic propagation of Wadsley defects and Magnéli phase under electrical field and shed light on the underlying mechanisms of field-induced high-density defects in FS ceramics.

Conflicts of interest

The authors declare that they have no known competing financial interests or personal relationships that could have appeared to influence the work reported in this paper.

Acknowledgement

The work is supported by the U.S. Office of Naval Research (Contract No N00014-17-1-2087 and N00014-22-1-2160 for sintering effort and N00014-20-1-2043 for *in situ* TEM). We would like to acknowledge access to the Life Science Microscopy Facility and the microscopy center of the School of Materials Engineering at Purdue University.

References

1. J. Luo, *Scripta Materialia*, 2018, **146**, 260-266.
2. R. Todd, E. Zapata-Solvas, R. Bonilla, T. Sneddon and P. Wilshaw, *Journal of the European Ceramic Society*, 2015, **35**, 1865-1877.
3. J. Narayan, *Scripta Materialia*, 2013, **69**, 107-111.
4. C. A. Grimley, A. L. Prette and E. C. Dickey, *Acta Materialia*, 2019, **174**, 271-278.
5. M. Biesuz, L. Pinter, T. Saunders, M. Reece, J. Binner, V. M. Sglavo and S. Grasso, *Materials*, 2018, **11**, 1214.
6. H. Charalambous, S. K. Jha, H. Wang, X. L. Phuah, H. Wang and T. Tsakalakos, *Scripta Materialia*, 2018, **155**, 37-40.
7. M. Biesuz and V. M. Sglavo, *Scripta Materialia*, 2018, **150**, 82-86.
8. H. Yoshida, K. Morita, B.-N. Kim, Y. Sakka and T. Yamamoto, *Acta Materialia*, 2016, **106**, 344-352.
9. W. Rheinheimer, X. L. Phuah, H. Wang, F. Lemke, M. J. Hoffmann and H. Wang, *Acta Materialia*, 2019, **165**, 398-408.
10. M. Blanchin, L. Bursill and C. Lafage, *Proceedings of the Royal Society of London. A. Mathematical Physical Sciences*, 1990, **429**, 175-202.
11. J. J. Cho, Q. Li, H. Wang, Z. Fan, J. Li, S. C. Xue, K. S. N. Vikrant, H. Y. Wang, T. B. Holland, A. K. Mukherjee, R. E. Garcia and X. H. Zhang, *Nature Communications*, 2018, **9**, 9.

12. J. Li, J. Cho, J. Ding, H. Charalambous, S. C. Xue, H. Wang, X. L. Phuah, J. Jian, X. J. Wang, C. Ophus, T. Tsakalakos, R. E. Garcia, A. K. Mukherjee, N. Bernstein, C. S. Hellberg, H. Y. Wang and X. H. Zhang, *Science Advances*, 2019, **5**, 9.
13. Y. Yamashita, T. Kurachi, T. Tokunaga, H. Yoshida and T. Yamamoto, *Journal of the European Ceramic Society*, 2020, **40**, 2072-2076.
14. Q. Li, S. C. Xue, Y. F. Zhang, X. Sun, H. Y. Wang and X. H. Zhang, *International Journal of Plasticity*, 2020, **132**, 18.
15. H. Charalambous, S. K. Jha, K. H. Christian, R. T. Lay and T. Tsakalakos, *Journal of the European Ceramic Society*, 2018, **38**, 3689-3693.
16. B. Yang, X. L. Phuah, Z. Shang, X. Sheng, H. Wang and X. Zhang, *Scripta Materialia*, 2022, **207**, 114270.
17. H. Bicer, B. Beyoglu, T. E. Ozdemir, J. Okasinski and T. Tsakalakos, *Ceram. Int.*, 2019, **45**, 7614-7618.
18. S. K. Jha, H. Charalambous, H. Wang, X. L. Phuah, C. Mead, J. Okasinski, H. Wang and T. Tsakalakos, *Ceram. Int.*, 2018, **44**, 15362-15369.
19. D.-H. Kwon, K. M. Kim, J. H. Jang, J. M. Jeon, M. H. Lee, G. H. Kim, X.-S. Li, G.-S. Park, B. Lee and S. Han, *Nature nanotechnology*, 2010, **5**, 148-153.
20. R. J. Kamaladasa, A. A. Sharma, Y.-T. Lai, W. Chen, P. A. Salvador, J. A. Bain, M. Skowronski and Y. N. Picard, *Microscopy and Microanalysis*, 2015, **21**, 140-153.
21. Z. Fan, J. Li, Y. C. Yang, J. Wang, Q. Li, S. C. Xue, H. Y. Wang, J. Lou and X. H. Zhang, *Advanced Materials Interfaces*, 2017, **4**, 9.
22. L. Bursill, B. Hyde, O. Terasaki and D. Watanabe, *Philosophical Magazine*, 1969, **20**, 347-359.
23. L. Bursill and B. Hyde, *Progress in solid state chemistry*, 1972, **7**, 177-253.
24. P. A. Cox, *Transition metal oxides: an introduction to their electronic structure and properties*, Oxford university press, 2010.
25. S. Andersson and A. D. Wadsley, *Nature*, 1966, **211**, 581-583.
26. K. Szot, M. Rogala, W. Speier, Z. Klusek, A. Besmehn and R. Waser, *Nanotechnology*, 2011, **22**, 254001.
27. A. Moballegh and E. C. Dickey, *Acta Materialia*, 2015, **86**, 352-360.
28. J. Kwon, A. A. Sharma, J. A. Bain, Y. N. Picard and M. Skowronski, *Advanced Functional Materials*, 2015, **25**, 2876-2883.
29. J. Anderson and B. Hyde, *Journal of Physics Chemistry of Solids*, 1967, **28**, 1393-1408.
30. C. Jia, M. Lentzen and K. Urban, *Science*, 2003, **299**, 870-873.
31. D. S. Jeong, R. Thomas, R. Katiyar, J. Scott, H. Kohlstedt, A. Petraru and C. S. Hwang, *Reports on progress in physics*, 2012, **75**, 076502.
32. D. S. Jeong, H. Schroeder, U. Breuer and R. Waser, *Journal of applied physics*, 2008, **104**, 123716.
33. J. Blanc and D. L. Staebler, *Physical Review B*, 1971, **4**, 3548.
34. R. Waser, T. Baiatu and K. H. Härdtl, *Journal of the American Ceramic Society*, 1990, **73**, 1645-1653.
35. W. Jiang, M. Noman, Y. Lu, J. Bain, P. Salvador and M. Skowronski, *Journal of Applied Physics*, 2011, **110**, 034509.
36. H.-I. Yoo, M.-W. Chang, T.-S. Oh, C.-E. Lee and K. Becker, *Journal of Applied Physics*, 2007, **102**, 093701.
37. T. Bak, J. Nowotny and M. Nowotny, *The Journal of Physical Chemistry B*, 2006, **110**, 21560-21567.
38. M. Nowotny, T. Bak and J. Nowotny, *The Journal of Physical Chemistry B*, 2006, **110**, 16270-16282.

39. M. K. Nowotny, L. R. Sheppard, T. Bak and J. Nowotny, *The Journal of Physical Chemistry C*, 2008, **112**, 5275-5300.
40. E. Cho, S. Han, H.-S. Ahn, K.-R. Lee, S. K. Kim and C. S. Hwang, *Physical Review B*, 2006, **73**, 193202.
41. P. Kofstad, *Journal of Physics Chemistry of Solids*, 1962, **23**, 1579-1586.
42. H. Iddir, S. Öğüt, P. Zapol and N. D. Browning, *Physical Review B*, 2007, **75**, 073203.
43. R. Hasiguti, *Annual Review of Materials Science*, 1972, **2**, 69-92.
44. L. A. Bursill and D. J. Smith, *Nature*, 1984, **309**, 319-321.
45. E. Yagi and R. R. Hasiguti, *Journal of the Physical Society of Japan*, 1977, **43**, 1998-2005.
46. M. Aono and R. Hasiguti, *Physical Review B*, 1993, **48**, 12406.
47. M. Blanchin and L. Bursill, *physica status solidi*, 1984, **86**, 101-109.
48. F. Millot, M. Blanchin, R. Tetot, J. Marucco, B. Poumellec, C. Picard and B. Touzelin, *Progress in solid state chemistry*, 1987, **17**, 263-293.
49. R. Waser, R. Dittmann, G. Staikov and K. Szot, *Advanced materials*, 2009, **21**, 2632-2663.
50. J. Smith, F. Walsh and R. Clarke, *Journal of applied electrochemistry*, 1998, **28**, 1021-1033.
51. B. F. Donovan, D. M. Long, A. Moballegh, N. Creange, E. C. Dickey and P. E. Hopkins, *Acta Materialia*, 2017, **127**, 491-497.
52. L. Liborio and N. Harrison, *Physical Review B*, 2008, **77**, 104104.
53. Y. Meng Lu, M. Noman, Y. N. Picard, J. A. Bain, P. A. Salvador and M. Skowronski, *Journal of Applied Physics*, 2013, **113**, 163703.
54. B. Yang, Z. Shang, J. Li, X.L. Phuah, J. Cho, H. Wang, X. Zhang, Journal of the European Ceramic Society, 2022, **42**, 6040-6047.
55. H. Wang, X.L. Phuah, H. Charalambous, S.K. Jha, J. Li, T. Tsakalakos, X. Zhang, H. Wang, Materialia, 2019, **8**, 100451.